

To appear in The Astrophysical Journal, v565 Jan 20, 2002 issue

A Chandra X-ray Study of Cygnus A — III. The Cluster of Galaxies

David A. Smith and Andrew S. Wilson¹

Department of Astronomy, University of Maryland, College Park, MD 20742;
dasmith@astro.umd.edu, wilson@astro.umd.edu

Keith A. Arnaud²

Laboratory for High Energy Astrophysics, NASA/GSFC, Code 662, Greenbelt, MD 20771;
kaa@genji.gsfc.nasa.gov

and

Yuichi Terashima³ and Andrew J. Young

Department of Astronomy, University of Maryland, College Park, MD 20742;
terasima@astro.umd.edu, ayoung@astro.umd.edu

ABSTRACT

We present an analysis of the *Chandra* Advanced CCD Imaging Spectrometer (ACIS) observation of the intracluster gas associated with the cluster of galaxies surrounding Cygnus A. The dominant gaseous structure is a roughly elliptical (presumably prolate spheroidal in three dimensions) feature with semi-major axis $\simeq 1'.1$ ($\simeq 100$ kpc). This structure apparently represents intracluster gas which has been swept up and compressed by a cavity inflated in this gas by relativistic material which has passed through the ends of the radio jets. The X-ray emitting gas shows this prolate spheroidal morphology to $\simeq 1'.2$ (110 kpc) from the radio galaxy, but is spherical on larger scales. The X-ray emission from the intracluster gas extends to at least $8'$ ($\simeq 720$ kpc) from the radio galaxy, and a second, extended source of X-ray emission (probably associated with a second cluster of galaxies) is seen some $12'$ ($\simeq 1$ Mpc) to the NW of Cygnus A. The X-ray spectrum of the integrated intracluster gas imaged on the S3 chip (dimensions $8' \times 8' = 720 \times 720$ kpc), excluding the contribution from the radio galaxy and other compact sources of X-ray emission, has a gas temperature, metallicity, and unabsorbed

¹Adjunct Astronomer, Space Telescope Science Institute, 3700 San Martin Drive, Baltimore, MD 21218; awilson@stsci.edu

²also Department of Astronomy, University of Maryland, College Park, MD 20742

³Institute of Space and Astronautical Science, 3-1-1 Yoshinodai, Sagamihara, Kanagawa 229-8510, Japan

2–10 keV rest-frame luminosity of 7.7 keV, 0.34 times solar, and 3.5×10^{44} erg s^{−1}, respectively.

We have deprojected the X-ray spectra taken from 12 elliptical and circular annuli in order to derive a run of temperature, metallicity, density, and pressure as a function of radius. The temperature of the X-ray emitting gas drops from $\simeq 8$ keV more than 100 kpc from the center to $\simeq 5$ keV some 80 kpc from the center, with the coolest gas immediately adjacent to the radio galaxy. “Belts” of slightly cooler ($\simeq 4$ keV) X-ray emitting gas run around the minor dimension of the cavity created by the radio source, while the limb-brightened edges of the cavity are slightly hotter ($\simeq 6$ keV), perhaps as a result of heating by a bow shock driven by the probably expanding cavity into the intracluster gas. There is a metallicity gradient in the X-ray emitting gas, with the highest metallicities (\sim solar) found close to the center, decreasing to ~ 0.3 solar in the outer parts. We have used the assumption of hydrostatic equilibrium to derive a total cluster mass within 500 kpc of $2.0 \times 10^{14} M_{\odot}$ and $2.8 \times 10^{14} M_{\odot}$ for a constant and centrally decreasing temperature profile, respectively. The total mass of X-ray emitting gas within the same radius is $1.1 \times 10^{13} M_{\odot}$. Thus, the gas fraction of the cluster within 500 kpc is 0.055 and 0.039 for the constant and centrally decreasing temperature profiles, respectively.

Subject headings: galaxies: abundances — galaxies: clusters: individual (Cygnus A) — galaxies: individual (Cygnus A) — intergalactic medium — X-rays: galaxies: clusters — X-rays: individual (Cygnus A)

1. Introduction

Cygnus A is the best known and nearest example ($z = 0.0562$) of a powerful FR II radio galaxy in a cluster of galaxies (e.g., Barthel & Arnaud 1996). At X-ray wavelengths, Cygnus A was first detected by Giacconi et al. (1972) using the *Uhuru* satellite. *Einstein* imaging data subsequently showed the radio source to reside in $10^{14} M_{\odot}$ of hot gas, extending some 1 Mpc (assuming $H_0 = 50$ km s^{−1} Mpc^{−1}) to the NW of Cygnus A (Arnaud et al. 1984). A dense core of hot gas, centered on the radio galaxy, was found to have an apparent cooling flow rate of $\sim 90 M_{\odot}$ yr^{−1} (Arnaud et al. 1984). *EXOSAT* and *HEAO-1* observations yielded a temperature of $kT \simeq 4$ –5 keV for the intracluster gas, with the radio galaxy modeled as an absorbed power-law (Arnaud et al. 1987). Subsequent observations with *Ginga* (Ueno et al. 1994) and *ASCA* (Sambruna, Eracleous, & Mushotzky 1999) gave a higher temperature of $kT \simeq 7$ –8 keV and an iron abundance of ~ 0.3 times solar. From *ROSAT* Position Sensitive Proportional Counter (PSPC) and High Resolution Imager (HRI) observations, Reynolds & Fabian (1996) suggest that the gas temperature within the inner 50 kpc is significantly cooler ($kT \simeq 2.5$ keV) than the ambient cluster temperature at radii $\gtrsim 180$ kpc, and that the cooling flow rate is $\sim 250 M_{\odot}$ yr^{−1}. In a recent analysis of the *ASCA* data, Markevitch et al. (1998) and Markevitch, Sarazin, & Vikhlinin (1999) have found evidence

for a merger between the two sub-clusters whose gas temperatures are $kT \simeq 4\text{--}5$ keV. The bi-modal redshift distribution of the galaxies in Cygnus A is also suggestive of a merger, although the density of galaxies does not correspond well to the distribution of X-ray emitting gas (Owen et al. 1997). From an analysis of the undeconvolved *ASCA* Gas Imaging Spectrometer data, White (2000) derived the overall cluster temperature and iron abundance to be 9.49 ± 0.23 keV and 0.67 ± 0.03 solar, respectively. The data were also modeled with a strong cooling flow of $\approx 500 M_{\odot} \text{ yr}^{-1}$, a high ambient cluster temperature of ≈ 40 keV, and a metallicity close to solar values.

This paper is devoted to a *Chandra* study of the intracluster gas in the Cygnus A cluster of galaxies. The morphology and radial profile of the X-ray emitting gas are discussed in Sections 3.1 and 3.2. In Sections 3.3 and 3.4, we derive the spectra of the gas and the observed radial dependences of the temperature and abundance. Section 3.5 is devoted to a deprojection of the observed spectral brightness distribution, providing the radial dependences of the temperature, abundance, emissivity, density, and pressure of the intracluster gas. These parameters are then used (Section 3.6) to obtain the distributions of the gas mass and total mass of the cluster. In Section 3.7, we discuss the extended filaments and belts of X-ray emission around the cavity in the intracluster gas which has been created by the radio source. Conclusions are summarized in Section 4.

We adopt $H_0 = 50 \text{ km s}^{-1} \text{ Mpc}^{-1}$ and $q_0 = 0$ in this paper, which gives $1'' = 1.51 \text{ kpc}$, an angular size distance of $d_A = 310.5 \text{ Mpc}$, and a luminosity distance to Cygnus A of $d_L = 346.4 \text{ Mpc}$.

2. Observations and Data Reduction

Cygnus A has been observed on three occasions with the *Chandra* ACIS (ACIS is described by G. Garmire et al., in preparation). The results from an analysis of the radio hot spots (Wilson, Young, & Shopbell 2000, hereafter Paper I) and the central nucleus (Young et al. 2001, hereafter Paper II) are presented elsewhere. The rationale for the three observations is described in Paper II.

We concern ourselves here with a study of the surrounding intracluster gas, and analyze only data acquired during the $\simeq 35$ ks exposure on May 21, 2000 (obsid 360), which provided an observation of Cygnus A over a wide field. The data reduction and analysis were done using *Chandra Interactive Analysis of Observations (CIAO)* software version 2.1, and the reprocessed (on January 25, 2001) event files. We created a new level 2 events file, applying the latest gain corrections (of January 25, 2001), the same Good Time Intervals as in the existing level 2 events file, and *ASCA* grades 0, 2, 3, 4, and 6. Periods of non-quiet background (i.e., flares or data dropouts due to telemetry saturation) were removed from the data. This was achieved by creating a light curve of the whole S3 chip, excluding the brightest sources of X-ray emission, and removing events $\pm 3\sigma$ from the mean count rate. This gives an effective exposure time of 34.3 ks (corrected for dead-time in the detector).

The X-ray emission from the cluster extends over the whole S3 chip, so our analysis procedure

followed that described in Markevitch et al. (2000). Spatial variations in the detector background were estimated from several ACIS blank-field observations⁴ with a total exposure of $\simeq 137$ ks on the S3 chip. These data were taken at the same focal plane temperature as our *Chandra* observation (i.e., -120°C). In the 10–11 keV band, where few or no cosmic X-rays are expected, the observed count rate is $5 \pm 1\%$ higher in our observation than in the blank field observations (where the quoted error is only the random component). This excess count rate is comparable with the systematic error in the background rate from field to field (Markevitch et al. 2000). Therefore, in the following sections, we have used a background rate that is 5% higher than the value obtained from the blank field observations. Finally, an exposure map for the S3 chip was created from knowledge of the satellite pointing direction and the effective area across the detector.

In Section 3.5, we present a deprojection of the X-ray emission of the cluster gas associated with Cygnus A. In brief, we derive the radial temperature, abundance, and emissivity using the XSPEC mixing model “project”⁵ written by one of us (KAA). This mixing model sums model spectra from ellipsoidal shells to give the observed, projected spectral emission of each elliptical annulus. The number of ellipsoidal shells is taken to be the same as the number of annuli, with each shell projecting onto one annulus. In the inner regions of the cluster, the shells are assumed to be prolate, with the major axis in the plane of the sky. In the outer regions, the shells are spherical. Thus, there are no free parameters associated with the geometry. The “project” model allows the annuli to have different semi-major axes, semi-minor axes, and orientations but they are required to have the same centroid.

3. Results

3.1. Morphology of The Extended X-ray Emission

An unsmoothed *Chandra* X-ray image of the region of the radio source Cygnus A was shown in Figure 1 of Paper I (see also Figure 11 of present paper). An alternative representation can be obtained by adaptively smoothing the image (the *CIAO* program CSMOOTH). In this process, the width of the two-dimensional Gaussian smoothing profile is a function of the signal to noise ratio of the data. Pixels with signal $> 5\sigma$ above the local background were left unsmoothed while for the remaining pixels, the width of the Gaussian was increased until the convolved signal at that location exceeded the local background by 3σ . The resulting image is shown in Figure 1.

Inspection of the unsmoothed (Figure 1 of Paper I; Figure 11 of present paper) and smoothed (Figure 1) images reveals the following features (see Wilson, Young, & Shopbell 2001 for an earlier summary). The dominant structure is a roughly elliptical (presumably prolate spheroidal in 3-d)

⁴See <http://hea-www.harvard.edu/~maxim/axaf/acisbg/> for further details regarding the ACIS background fields.

⁵Publicly available in XSPEC v11.1

feature with semi-major axis $\simeq 1.1$. The major axis coincides well with that of the radio source, and the radio hot spots are seen as compact X-ray sources at the ends of the major axis (Paper I). This structure appears to be the observational manifestation of the intracluster gas which has been swept up and compressed by a cavity which is expected to be inflated in the intracluster gas by relativistic material which has passed through the hot spots at the ends of the jets (Scheuer 1974). X-ray emission around the cavity seems to be edge-brightened. Curved linear structures run along the major axis from the nucleus to each pair of hot spots and may be the X-ray manifestations of the jets; they will not be discussed further in this paper. There is extended X-ray emission associated with the nucleus (Paper II). Bright curved bands of X-ray emission extend along the minor axis of the ellipse. Their morphology, particularly in the unsmoothed image, is suggestive of “belts” of gas extending around the equator of the prolate spheroidal structure. Since the dominant radio jet is on the NW side of the nucleus, it is usually supposed that this is the near side of the radio source. If the “belts” are circular and in the equatorial plane of the cavity, their sense of curvature indicates that they are predominantly on the far side. The reason for the absence of belts curved concave to the NW (as would be expected for the near side gas) is unclear. As we shall see (Section 3.7), the belts are gas with a temperature of $\simeq 4$ keV and could represent a large-scale accretion disk, with gas flowing in to Cygnus A. The existence of the cavity and evidence for its edge-brightening was inferred from lower resolution *ROSAT* HRI observations by Carilli et al. (1994) and a numerical simulation of its dynamics was presented by Clarke et al. (1997). A more detailed analysis of the cavity will be presented elsewhere (Wilson & Smith 2002).

An image of the X-ray emission on chip S3 (size $8' \times 8'$) is shown in Figure 2. The background has been subtracted from the raw image and the result has been corrected for variations in vignetting and relative exposure. The final image has been convolved with a two-dimensional Gaussian profile of width $\sigma = 5$ pixels ($= 2''.46$). The radio galaxy is located towards the upper right, at the aimpoint of the S3 chip. It is clear from this image that the spatial extent of the X-ray emitting gas is larger than the field of view of the S3 chip, as already known from earlier observations (e.g., Reynolds & Fabian 1996). In addition to the galaxy nucleus and radio hot spots, a total of 19 compact sources were detected on the S3 chip with a significance threshold of 10^{-6} using the *CIAO* program WAVDETECT⁶. However, none of the galaxies listed in Table 1 of Owen et al. (1997), and visible within the field of view of the S3 chip, was detected. We conclude that these compact X-ray sources are most likely foreground (e.g., stars) or background (e.g., AGN) objects.

An image of the whole *Chandra* field is shown in Figure 3. This image has been binned to a pixel size of $3''.94 \times 3''.94$. The bright source near the center of the image is Cygnus A. The X-ray emission from the intracluster gas extends at least $8'$ from the radio galaxy. A second, fainter source of extended X-ray emission is seen some $12'$ to the NW of Cygnus A, and is partially obscured by

⁶A significance threshold of 10^{-6} will give approximately one false source for the whole S3 chip (see Section 9.2.3.4 of the Detect User’s Guide version 1.0 which is available at <http://xc.harvard.edu/udocs/docs/swdocs/detect/html/MDETECT.html>)

the boundary dividing the S1 and S2 chips. This second source was detected by *ROSAT* (Reynolds & Fabian 1996) and by *ASCA* (Markevitch et al. 1998, 1999). It is natural to presume that this second extended source represents another cluster of galaxies (see Markevitch et al. 1999). There is also evidence for extended X-ray emission between the two clusters.

3.2. Radial Profile of the Intracluster Gas

A radial profile of the X-ray surface brightness was determined by extracting, from the S3 chip, counts in the 0.75–8 keV band in circular annuli of width 5 pixels ($= 2''.46$) and centered on the radio galaxy. We have ignored deviations in the symmetry due to the prolate morphology of the intracluster gas in the inner regions of the cluster. A similar approach to that used in making Figure 2 was adopted for removal of background and correction for telescope vignetting. For regions of the chip within $1'.23$ of the radio galaxy, the annuli were restricted to two pie-shaped regions some 50° and 70° in angular extent, chosen to avoid emission near the radio lobes and hot spots. In the outer regions of the chip, compact sources of X-ray emission were excluded from the radial profile. The final profile has been binned so that the signal to noise ratio in each bin exceeds 25 (Figure 4).

The radial surface brightness profile, $S(\theta)$, has been modeled by an isothermal β profile (Sarazin & Bahcall 1977):

$$S(\theta) = S_o \times [1 + (\theta/\theta_c)^2]^{-3\beta+0.5}, \quad (1)$$

where S_o , θ , θ_c , and β are the central surface brightness, angular distance from the center, the angular core radius, and the slope parameter, respectively. In fitting the model, we have used only data at radii $6''$ – $16''$ and $\geq 37''$, chosen to avoid, as much as possible, the increase in surface brightness around the edge of the cavity and at the nucleus of the radio galaxy. The model provides a poor description of the profile even when these anomalous regions are excluded, with $\chi^2 = 111.5$ for 51 degrees of freedom (d.o.f.); the best-fit parameters are $\theta_c \simeq 18$ arcsec and $\beta \simeq 0.51$. We note that the isothermal β profile is flat inside θ_c , and thus small values of θ_c may indicate that there is emission in excess of that expected from the ambient intracluster gas. Carilli et al. (1994) determined $\theta_c = 35 \pm 5$ arcsec and $\beta = 0.75 \pm 0.25$, using the *ROSAT* HRI data at radii $\geq 6''$. If we restrict our analysis to the data within radii $6''$ – $90''$, the same radial extent as that used in Carilli et al. (1994), then we find $\theta_c \simeq 29''$ and $\beta \simeq 0.67$. An isothermal β profile with these parameters, when extrapolated to larger radii, underestimates the X-ray surface brightness.

The data have also been modeled with the analytic expression of Suto, Sasaki, & Makino (1998) for the Navarro et al. (1996, 1997, hereafter NFW) profile:

$$S(\theta) = S_o \times [1 + (\theta/\theta_c)^\xi]^{-\eta}, \quad (2)$$

where $\xi = -4.99 + 7.055 \times B^{-1/30}$ and $\eta = -0.68 + 0.2226 \times B^{1.1}$. The parameter B is $(4\pi G \mu m_p \delta_c \rho_{c0} r_s^2)/kT$, where δ_c is the characteristic density of the cluster, ρ_{c0} is the critical density of the universe at

redshift $z = 0$, r_s is the characteristic scale radius of the cluster, μ is the mean molecular weight ($\mu = 0.6$ if no metals present), m_p is the mass of the proton, k is Boltzmann’s constant, T is the temperature of the gas, and G is the gravitational constant (Suto et al. 1998). This model also provides a poor description of the profile (again, the anomalous regions were omitted) with $\chi^2 = 145.6$ for 51 d.o.f.; the best-fit parameters are $\theta_c \simeq 17$ arcsec and $B \simeq 7.4$. The NFW profile may not be an accurate description of the density of the dark matter halo within the inner regions of the cluster, due to the poor spatial resolution of the N -body simulations (Fukushige & Makino 1997; Moore et al. 1998). However, we have also tried to model the data with a generalized form of the profile, in which ξ and η are free parameters, without success. It is possible that the central $30''$ region of the cluster are not in hydrostatic equilibrium (there a powerful radio source located at the center of the cluster) or that the X-ray surface brightness increases towards the center of the cluster as a result of a cooling flow, which would explain why the data are not described by either the isothermal β or NFW profiles. Unfortunately, modeling the data at radii $\geq 37''$ does not allow a determination of the core radius for either description of the profile. Instead, a power-law of $S(\theta) \propto \theta^{-1.993 \pm 0.016}$ (errors here and elsewhere in this paper are 90% confidence for one interesting parameter, $\Delta\chi^2 = 2.706$) provides a reasonable description of the profile with $\chi^2 = 66.3$ for 48 d.o.f.

3.3. Spectra of the Intracluster Gas

The spectral variations in the intracluster gas are illustrated in Figure 5, which is a color map of the softness ratio (1–2 keV/2–8 keV) for the same region as shown in Figure 2. We have extracted images in the 1–2 keV and 2–8 keV bands, as input to the program ADAPTIVEBIN version 0.1.2 (Sanders & Fabian 2001). The resulting color image was adaptively binned so that the maximum fractional error in the color was 0.1 at each location (see color bar on right of Figure 5). Background was subtracted from the images, so that the colors represent the softness ratios of the celestial X-ray emission. The color image shows that emission inside the central $\simeq 1'$ is softer than that further out. The hardest emission is located at the position of the nucleus, which is heavily absorbed (Arnaud et al. 1987; Ueno et al. 1994; Sambruna et al. 1999; Paper II).

Our goal in this paper is to investigate the spatial variations of the properties (e.g., density, temperature, and abundances) of the intracluster gas in the inner region of the Cygnus A cluster (i.e., that which falls on chip S3 in our observation). We began by extracting spectra from several annuli centered on the radio galaxy (see Figure 6) using PI channels, which account for variations in the gain across each of the extraction regions. We created response matrices appropriate for our spectra by weighting the position dependent response and effective area by the number of counts in the corresponding region. Care was taken to avoid emission powered by the radio galaxy itself; this is the reason only sectors of elliptical annuli (Figure 6) were used in the inner regions (see Table 1 for the parameters of the ellipses used for each annulus). The angular extents of the sectors used for the outer annuli were limited by the size of the CCD chip (Figure 2).

Initially, the spectrum of *all* the intracluster gas within the S3 chip, excluding the contribution from the radio galaxy and other compact sources of X-ray emission, was modeled by an absorbed, single temperature mekal (Mewe et al. 1995), using XSPEC version 11.0.1 (Arnaud 1996). The absorption cross-sections of Morrison & McCammon (1983) and abundances of Anders & Grevesse (1989) were used throughout. This model (model 1) gives a poor fit to the data with $\chi^2 = 736.2$ for 489 d.o.f. (see Table 2). The best-fit temperature, metallicity, and equivalent hydrogen absorbing column density are $kT \simeq 8.3$ keV, $Z \simeq 0.35 Z_\odot$, and $N_H \simeq 2.8 \times 10^{21} \text{ cm}^{-2}$, respectively. The combined spectrum, together with the residuals to this model fit, are shown in Figure 7. There are large residuals near the M-edge of iridium, which arises from X-ray absorption in the telescope mirror surface. Large residuals near the iridium M-edge were also found in the spectra of two high temperature clusters, A665 and A2163, observed with the front-illuminated CCDs on *Chandra* (Markevitch & Vikhlinin 2001). Ignoring the data between 1.8 and 2.2 keV (as Markevitch & Vikhlinin have done) gives a better, although still unacceptable, fit of $\chi^2 = 548.2$ for 461 d.o.f., with the observed temperature, metallicity, and absorbing column density essentially unchanged from their former values. For comparison, the Medium Energy experiment on *EXOSAT* measured a temperature of $4.1^{+5.6}_{-1.5}$ keV and an iron abundance of $0.59^{+0.68}_{-0.35}$ times solar for the intracluster gas (Arnaud et al. 1987). Similarly, a temperature of $7.3^{+1.8}_{-1.3}$ keV and an iron abundance of $\simeq 0.32$ times solar were found from spectral fits to the *Ginga* Large Area Counter data (Ueno et al. 1994). Both of these experiments used non-imaging proportional counters, which included in their field of view emission from both the radio galaxy and the intracluster gas outside chip S3. More recent observations with *ASCA*, which also refer to a larger region than ours, measured the overall cluster temperature and abundance to be $kT \simeq 8$ keV and ~ 0.6 times solar, respectively (Markevitch et al. 1998, 1999; Sambruna et al. 1999; White 2000).

There is evidence from *ASCA* observations of clusters for an Si/Fe abundance ratio which increases with increasing gas temperature (Fukazawa et al. 1998). An increase in the Si/Fe abundance would produce more line emission at 1.84–1.86 (Si XIII), 2.01 (Si Ly α), and 2.38 (Si Ly β) keV, which may contribute to the positive residuals near the iridium M-edge. Thus, we have replaced the mekal model with a vmekal model, in which H and He have solar abundances, C and N have 0.3 solar abundances, and the remaining metals are permitted to have variable abundances. This model provides a slightly better description of the data than model 1 with $\chi^2 = 726.6$ for 479 d.o.f. The best-fit temperature, Si abundance, Fe abundance, and equivalent hydrogen absorbing column density are $kT \simeq 8.3$ keV, $Z(\text{Si}) \simeq 0.38 Z_\odot$, $Z(\text{Fe}) \simeq 0.33 Z_\odot$, and $N_H = 2.8 \times 10^{21} \text{ cm}^{-2}$, respectively. The Si/Fe abundance ratio is $\simeq 1.1$, which is smaller than that observed in other clusters with a similar gas temperature (Mushotzky et al. 1996; Fukazawa et al. 1998). Thus, an increased Si/Fe abundance ratio is not required by the data, but the inaccuracies in the response matrix at the energy of the Si line emission makes an accurate determination of the Si/Fe abundance ratio difficult. For the remainder of this paper, we shall assume a Si/Fe abundance ratio of unity.

The Galactic column density towards Cygnus A is $N_H(\text{Gal}) = 3.5 \times 10^{21} \text{ cm}^{-2}$ (Dickey & Lockman 1990), which is higher than that inferred from model 1. One possibility is that the

Galactic column density is lower than that estimated from Dickey & Lockman’s observations. Another explanation for this discrepancy is that the soft X-ray response of the detector is lower than assumed. However, we have used only data above 0.75 keV, where the ACIS S3 chip is well calibrated. Additionally, when the radial dependence of the column density was first derived (see Section 3.4), we found that the best-fit column density decreased with increasing distance from the radio galaxy, reaching $N_{\text{H}} \simeq 1.8 \times 10^{21} \text{ cm}^{-2}$ at the outer annulus. This effect could represent a real variation in the column density. Alternatively, given the low Galactic latitude of Cygnus A ($b = 5.^\circ 76$), this apparent spatial dependence of N_{H} could result from the presence of diffuse, soft X-ray emission from our Galaxy. To test this idea, we have added to model 1 a second mekal component, with solar abundances, to represent this possible Galactic emission, with both mekals constrained to be absorbed by the same column density (model 2). The improvement in the fit compared with that for model 1 is significant at $> 99\%$ confidence (on the basis of an F test for two additional free parameters), with $\chi^2 = 709.4$ for 487 d.o.f.; the best-fit parameters are given in Table 2. The observed 0.75–8 keV flux of the high temperature, cluster component is $2.7 \times 10^{-11} \text{ erg cm}^{-2} \text{ s}^{-1}$. There is no improvement (at $> 90\%$ confidence) in the fit when we allow the abundance of the low temperature, Galactic thermal component to vary. The observed surface brightness of this possible Galactic thermal component is $5.2 \times 10^{-15} \text{ erg s}^{-1} \text{ cm}^{-2} \text{ arcmin}^{-2}$ in the 0.75–8 keV band.

3.4. Observed radial dependence of temperature, abundance, and emissivity

The next step was to model the individual annuli with an absorbed mekal. We assumed there is little variation in the Galactic column over the cluster, and so assumed the same column for all annuli. Two mekal components were used for each annulus. The first was assumed to have uniform temperature, surface brightness, and abundance (fixed at solar), and was taken to represent the possible foreground Galactic emission (see Section 3.3). The second, intended to represent the cluster, permitted variable temperature, abundance, and brightness, to derive the radial variations of these properties in the cluster. The results from this model, in which all annuli were fitted simultaneously, are given in Table 3. We note that variations in the absorption column density are not required by the data for this model. The inferred intracluster gas temperature varies from $\sim 8 \text{ keV}$ more than $\sim 2'$ from the center to $\simeq 5 \text{ keV}$ some $30''$ from the center, with the coolest gas immediately adjacent to the cavity created by the radio galaxy (Figure 8a). This temperature variation is compatible with the softness ratio map in Figure 5. There is also clear evidence for a metallicity gradient in the X-ray emitting gas, with the highest metallicities (~ 0.6 – 0.8 solar) found in the inner annuli, decreasing to ~ 0.3 solar in the outer parts (Figure 8b).

It is interesting to compare these results with those obtained previously. From the *ROSAT* PSPC data, Reynolds & Fabian (1996) find evidence for $2.5^{+0.7}_{-0.4} \text{ keV}$ gas within $1'$ of the radio nucleus. Their temperature is lower than that determined from our modeling of the individual annuli. However, we note that there is evidence for gas at a temperature of $\simeq 4 \text{ keV}$ in the “belts”

around the cavity (see Section 3.7 below), which is marginally consistent with their upper limit; in fact, the PSPC spectrum within $1'$ of the nucleus may be dominated by the emission from this 4 keV gas. The temperature derived from the PSPC data at radii ≥ 100 kpc is consistent with the values determined from the *Chandra* data. Using *ASCA* data, Markevitch et al. (1999) have constructed a map of the projected gas temperature within the Cygnus A cluster. However, their map has poor spatial resolution, with most of the intracluster gas within the S3 chip residing in region 1. Markevitch et al. (1999) measured a gas temperature in the range $\simeq 5$ to $\simeq 7$ keV for X-ray emission within this region, which is consistent with the temperature of the integrated intracluster gas on S3 (Section 3.3). Markevitch et al. (1999) identified regions of potentially higher and lower gas temperatures, but most of this emission resides on the other *Chandra* CCDs. White (2000) has performed a re-analysis of the *ASCA* data, and finds that the gas has a temperature in the range $\simeq 6$ to $\simeq 8$ keV in the region covered by the S3 chip, and a metallicity of $\simeq 0.2$ – 0.3 solar.

3.5. Deprojected radial dependence of temperature, abundance, and emissivity

The X-rays observed from each annulus contain emission from all gas along our line of sight in that direction. Thus, to obtain the physical parameters of the thermal gas as a function of distance from the center, it is necessary to deproject the observed spectral brightness distribution. In performing this deprojection, we have assumed that the X-ray emission from the cluster around the radio galaxy is distributed in a series of prolate ellipsoidal shells, whose major axis is along the projected radio jet axis at a position angle (P.A.) of $\simeq 116.^{\circ}3$ and is in the plane of the sky. Guided by the X-ray isophotes (Figure 2), we assumed that the ellipticity of these shells steadily decreases until the shells become spherical some $2'.5$ from the center. We feel this geometry is likely to be a good approximation to that of the intracluster gas in this inner part of the cluster (there is an extension $\sim 12'$ to the NW, but this region is not on chip S3). As a narrow line radio galaxy, the radio jet and lobes of Cygnus A are expected to be close to the plane of the sky, a geometry favored by Hargrave & Ryle (1974) on independent grounds. Carilli et al. (1996) state that the average ejection angle could be $\phi > 60^{\circ}$ from our line of sight, while Sorathia et al. (1996) favor $55^{\circ} < \phi < 80^{\circ}$ based on VLBI observations. Thus our assumption that the major axis of the the prolate spheroid lies in the plane of the sky may not be too far wrong. One limitation of our analysis is that our outer annulus (Figure 6) does not represent the true edge of the intracluster emission (cf. Reynolds & Fabian 1996), so there will be faint, more extended intracluster emission projected onto it.

As described in Section 2, we deprojected the observed emission using the XSPEC model “project”. Each shell was modeled as a mekal (thermal) plasma. The spectral analysis was performed in the following way. First, a uniform brightness mekal model (representing the Galactic emission) was added to a mekal model for the outer shell and the projected result was compared with the observed spectrum of the outer annulus (annulus 12). Both emission components were assumed to be absorbed by the same column and the model parameters for absorption and Galactic emission were

subsequently fixed at their respective best-fit values given in Table 3. In this way, we derived the temperature, abundance, and emissivity for the outer shell of intracluster gas. Second, the spectra from shells 11 and 12 were modeled as above. The temperature, abundance, and emissivity for shell 12 were fixed at the values already obtained, allowing us to derive the deprojected temperature, abundance, and emissivity for shell 11. This procedure was repeated for the remaining shells, and the results for all shells are given in Table 4. An alternative approach would be to sequentially model the various annuli, but to allow their parameters to be free in the final fitting in which all the projected mekal models are compared with the data. This approach has the disadvantage that the final modeling is insensitive to the fainter outer regions, for which the derived parameters are thus unreliable. For this reason, we consider our approach, in which one annulus is added at each modeling and then “frozen” in subsequent iterations, to be superior.

The properties of the intracluster gas for each of the spheroidal or spherical shells are given in Table 5. The properties of the gas in the outer shell (shell 12) are not listed since the volume of this shell is smaller than the volume of the intracluster gas projected onto it, rendering the calculated properties unreliable. The pressure and cooling time of the gas are $n_e kT$ and $n_e kTV/L_X$, respectively. We have used the usual notation here, in which n_e is the electron density, V is the volume of the shell, and L_X is the 2–10 keV rest-frame luminosity after correcting for absorption. In Figure 9, we show the radial dependence of deprojected temperature, electron density, abundance, and gas pressure. The peak in gas pressure between 90 and 100 kpc is not significant given the errors on the temperature at this location. The deprojected and observed temperatures and abundances are consistent with each other, which suggests that the emission observed in the inner regions of the cluster dominates the fainter outer emission projected onto it. It is notable that the cooling time is less than the Hubble time for radii $\lesssim 200$ kpc.

3.6. Distribution of Mass in the Cluster

Under the assumption of hydrostatic equilibrium and spherical symmetry of the inter-cluster gas, the mass of the cluster, M , within a radius, r , is

$$M(< r) = -\frac{kT(r)r^2}{\mu m_p G} \left(\frac{1}{n_e} \frac{dn_e}{dr} + \frac{1}{T} \frac{dT}{dr} \right) \quad (3)$$

(e.g., Fabricant, Lecar, & Gorenstein 1980), where $T(r)$ is the temperature at radius r . We have considered two alternative descriptions of the temperature: (i) a constant temperature of 5.73 keV; (ii) a centrally decreasing profile of the form

$$T(\text{keV}) = a - b \exp(-r(\text{kpc})/c), \quad (4)$$

where $a = 7.81$ keV, $b = 7.44$ keV, and $c = 76.4$ kpc are constants determined from modeling the deprojected temperatures. Hence, for the centrally decreasing temperature profile, the second term

in parentheses in Equation 3 may be written

$$\frac{1}{T} \frac{dT}{dr} = \frac{1}{T} \frac{b}{c} \exp(-r/c). \quad (5)$$

The radial dependence of the electron density has been modeled as a broken power-law of the form

$$n_e(\text{cm}^{-3}) = \begin{cases} w (r(\text{kpc})/x)^{-y} & : r > c \\ w (r(\text{kpc})/x)^{-z} & : \text{otherwise,} \end{cases} \quad (6)$$

where $w = 8.24 \times 10^{-3} \text{ cm}^{-3}$, $x = 97.2 \text{ kpc}$, $y = 1.50$, and $z = 4.11$ are the best-fit values. The slope of the density profile at large radii is consistent with an isothermal β profile of $\beta = 0.5$ (the electron density is $n_e \propto r^{-3\beta}$ for $r \gg \theta_c$). A similar value for β was derived directly from the X-ray surface brightness profile in Section 3.2. The first term in parentheses in Equation 3 may be written

$$\frac{1}{n_e} \frac{dn_e}{dr} = \begin{cases} -(y/x) (r/x)^{-1} & : r > c \\ -(z/x) (r/x)^{-1} & : \text{otherwise.} \end{cases} \quad (7)$$

Substituting Equations 5 and 7 into Equation 3 gives the integrated mass of the cluster, including the contributions from dark matter, intracluster gas, and individual galaxies. The radial dependence of enclosed mass $M(< r)$ is shown in Figure 10 for radii 80–500 kpc. We have also calculated the integrated mass of the intracluster gas, M_{gas} , (also shown in Figure 10) for the same range of radii, from

$$M_{\text{gas}}(< r) = \mu m_p \int n_e(r) dV, \quad (8)$$

where dV is the volume of the shell containing gas at density $n_e(r)$ (which is given by Equation 6). The integrated mass of gas within the inner 80 kpc of the cluster was determined by assuming a constant density of $n_e = w(80 \text{ kpc})/x)^{-z} = 0.018 \text{ cm}^{-3}$. From the above analysis, we find the total mass of the cluster, within 500 kpc, is $2.0 \times 10^{14} M_\odot$ and $2.8 \times 10^{14} M_\odot$ for the constant and centrally decreasing temperature profiles, respectively. This compares favorably with the cluster mass of $10^{14} M_\odot$, derived from the *Einstein* HRI data (Arnaud et al. 1984). Within 500 kpc, the total mass of the intracluster gas is $1.1 \times 10^{13} M_\odot$.

3.7. Extended Filaments and Belts of X-ray Emission near the Radio Source Cavity

Spectra were extracted from several regions of bright, extended X-ray emission near the nucleus (see Figure 11). The regions were chosen so that they included the curved belts of X-ray emission which appear to encircle the radio source cavity, as well as the bright bands of emission around the edge of the cavity. Care was taken to avoid the curved linear structures which extend from the nucleus to radio hot spots as these regions are apparently related to the radio activity which is

outside the scope of this paper. Prior to modeling, the spectra were re-binned so that there were at least 20 cts bin⁻¹ and the analysis was conducted over the full 0.5–10 keV band, as the diffuse, X-ray emission from our Galaxy is insignificant compared to this emission from these bright inner regions of the intracluster medium.

We have modeled each spectrum with a single temperature mekal, absorbed by a column of cold gas, which provides an acceptable fit to all 10 spectra (see table 6 for details). The gas associated with the regions of the curved belts (C, D, E, F, G, and I) has a temperature of $\simeq 4$ keV, which is cooler than that observed some 30'' from the center of the cluster (see Section 3.4 and Table 3). Gas located in the bands of X-ray emission around the edge of the cavity (regions A, B, H, and J) has a higher temperature of $\simeq 6$ keV, which is slightly higher than that inferred ($\simeq 5$ keV) in the adjacent, inner regions of the intracluster gas (Section 3.5 and Tables 3 and 4). This slightly higher temperature might result through heating of the gas by the probably expanding cavity, by means of the bow shock driven into the intracluster gas. The metallicities (~ 0.8 –1 solar) are consistent with, if somewhat higher than, those observed some 30'' from the center. There appears to be a slight gradient in the absorption column density, with the higher columns observed north of the nucleus. We note that there is no obvious relationship between measured column density and size of the corresponding extraction region, which would result if diffuse, X-ray emission from our Galaxy was significant. However, the uncertainties on the absorption column densities are comparable to the range of columns, so it is unclear whether this gradient is real.

4. Conclusions

We have analyzed the properties of the intracluster gas around Cygnus A using an observation with the ACIS-S aboard *Chandra*. The prolate morphology of the X-ray emission from the intracluster gas within $\simeq 2'$ of the radio galaxy appears to be the result of gas being swept up by a cavity created in the intracluster gas by the radio source. At larger radii, the X-ray emission from the intracluster gas appears to be roughly spherical, and extends at least 8' from the radio galaxy. A second, fainter source of extended X-ray emission is seen some 12' to the NW of Cygnus A. The radial X-ray surface brightness profile, $S(\theta)$, cannot be modeled by either an isothermal β model (Sarazin & Bahcall 1977) or the analytic expression of Suto et al. (1998) for the NFW (Navarro et al. 1996, 1997) profile. However, we find that the surface brightness at radii $\geq 37''$ is adequately described by a power-law $S(\theta) \propto \theta^{-1.993 \pm 0.016}$. The spectrum of the intracluster gas imaged on the S3 chip has been modeled by a mekal absorbed by a single column of cold gas. The temperature and unabsorbed 2–10 keV rest-frame luminosity of the intracluster gas imaged on S3 are 7.7 keV and 3.5×10^{44} erg s⁻¹, respectively. The equivalent hydrogen column density is 3.39×10^{21} cm⁻², close to the Galactic value, and the metallicity is 0.34 times solar. Although the data do not require an enhanced Si/Fe abundance ratio relative to solar, as detected in other clusters with similar gas temperatures (Fukazawa et al. 1998), the actual Si abundance is uncertain as a result of the inaccuracies in the response matrix at energies close to the iridium M-edge. We also suspect a Galactic

thermal component with temperature 0.67 keV and observed surface brightness $\simeq 5.2 \times 10^{-15}$ erg s $^{-1}$ cm $^{-2}$ arcmin $^{-2}$ in the 0.75–8 keV band.

We have deprojected the X-ray spectra taken from several elliptical and circular annuli centered on Cygnus A. The temperature of the X-ray emitting gas drops from $\simeq 8$ keV more than 100 kpc from the center to $\simeq 5$ keV some 80 kpc from the center, with the coolest gas immediately adjacent to the cavity. The bright “belts” of X-ray emission that appear to encircle the radio source cavity are somewhat cooler ($\simeq 4$ keV), while the “filaments” responsible for the limb-brightening of the cavity are slightly hotter (~ 6 keV), perhaps as a result of heating by a bow shock driven by the probably expanding cavity into the intracluster gas. A metallicity gradient is detected in the X-ray emitting gas, with the highest metallicities (\sim solar) found close to the center decreasing to ~ 0.3 solar in the outer parts. We have used the assumption of hydrostatic equilibrium to derive the total gravitational mass of the cluster as a function of radius. The total mass of the cluster within 500 kpc is $2.0 \times 10^{14} M_{\odot}$ and $2.8 \times 10^{14} M_{\odot}$ for a constant and centrally decreasing temperature profile, respectively. The total mass of X-ray emitting gas within the same radius is $1.1 \times 10^{13} M_{\odot}$. Thus, the gas fraction of the cluster within 500 kpc is 0.055 and 0.039 for the constant and centrally decreasing temperature profile, respectively.

This research was supported by NASA grant NAG 81027 and by a fellowship to ASW from the Graduate School of the University of Maryland. YT is supported by the Japan Society for the Promotion of Science Postdoctoral Fellowship for Young Scientists.

REFERENCES

- Anders, E., & Grevesse, N. 1989, *Geochimica et Cosmochimica Acta*, 53, 197
- Arnaud, K. A., Fabian, A. C., Eales, S. A., Jones, C., & Forman, W. 1984, *MNRAS*, 211, 981
- Arnaud, K. A., Johnstone, R. M., Fabian, A. C., Crawford, C. S., Nulsen, P. E. J., Shafer, R. A., & Mushotzky, R. F. 1987, *MNRAS*, 227, 241
- Arnaud, K. A. 1996, in *ASP Conf. Proc. 101, Astronomical Data Analysis Software and Systems V*, ed. G. Jacoby & J. Barnes (San Francisco: ASP), 17
- Barthel, P. D., & Arnaud, K. A. 1996, *MNRAS*, 283, L45
- Carilli, C. L., Perley, R. A., & Harris, D. E. 1994, *MNRAS*, 270, 173
- Carilli, C. L., Perley, R. A., Bartel, N., & Dreher, J. W. 1996, in *Cygnus A - Study of a Radio Galaxy*, ed. C. L. Carilli & D. E. Harris (Cambridge: Cambridge Univ. Press), 76
- Clarke, D. A., Harris, D. E., & Carilli, C. L. 1997, *MNRAS*, 284, 981
- Dickey, J. M., & Lockman, F. J. 1990, *ARA&A*, 28, 215

- Fabricant, D., Lecar, M., & Gorenstein, P. 1980, *ApJ*, 241, 552
- Fukazawa, Y., Makishima, K., Tamura, T., Ezawa, H., Xu, H., Ikebe, Y., Kikuchi, K., & Ohashi, T. 1998, *PASJ*, 50, 187
- Fukushige, T., & Makino, J. 1997, *ApJ*, 477, L9
- Giacconi, R., Murray, S., Gursky, H., Kellogg, E., Schreier, E., & Tananbaum, H. 1972, *ApJ*, 178, 281
- Hargrave, P. J., & Ryle, M. 1974, *MNRAS*, 166, 305
- Lampton, M., Margon, B., & Bowyer, S. 1976, *ApJ*, 208, 177
- Markevitch, M., Forman, W. R., Sarazin, C. L., & Vikhlinin, A. 1998, *ApJ*, 503, 77
- Markevitch, M., Sarazin, C. L., & Vikhlinin, A. 1999, *ApJ*, 521, 526
- Markevitch, M., et al. 2000, *ApJ*, 541, 542
- Markevitch, M., & Viklinin, A. 2001, *ApJ*, submitted (astro-ph/0105093)
- Mewe, R., Kaastra, J. S., Liedahl, D. A. 1995, *Legacy* 6, 16
- Moore, B., Governato, F., Quinn, T., Stadel, J., & Lake, G. 1998, *ApJ*, 499, L5
- Morrison, R., & McCammon, D. 1983, *ApJ*, 270, 119
- Mushotzky, R., Loewenstein, M., Arnaud, K. A., Tamura, T., Fukazawa, Y., Matsushita, K., Kikuchi, K., & Hatsukade, I. 1996, *ApJ*, 466, 686
- Navarro, J. F., Frenk, C. S., & White, S. D. M. 1996, *ApJ*, 462, 563
- Navarro, J. F., Frenk, C. S., & White, S. D. M. 1997, *ApJ*, 490, 493
- Owen, F. N., Ledlow, M. J., Morrison, G. E., & Hill, J. M. 1997, *ApJ*, 488, L15
- Reynolds, C. S., & Fabian, A. C. 1996, *MNRAS*, 278, 479
- Sambruna, R. M., Eracleous, M., & Mushotzky, R. F. 1999, *ApJ*, 526, 60
- Sanders, J. S., & Fabian, A. C. 2001, *MNRAS*, in press
- Sarazin, C. L., & Bahcall, J. N. 1977, *ApJS*, 34, 451
- Scheuer, P. A. G. 1974, *MNRAS*, 166, 513
- Sorathia, B., Bartel, N., Bretenholz, M. F., & Carilli, C. L. 1996, in *Cygnus A - Study of a Radio Galaxy*, ed. C. L. Carilli & D. E. Harris (Cambridge: Cambridge Univ. Press), 86

- Suto, Y., Sasaki, S., & Makino, N. 1998, *ApJ*, 509, 544
- Ueno, S., Koyama, K., Nishida, M., Yamauchi, S., Ward, M. J. 1994, *ApJ*, 431, L1
- White, D. A. 2000, *MNRAS*, 312, 663
- Wilson, A. S., Young, A. J., & Shopbell, P. L. 2000, *ApJ*, 544, L27 (Paper I)
- Wilson, A. S., Young, A. J., & Shopbell, P. L. 2001, in *Particles and Fields in Radio Galaxies*, ed. R. A. Laing & K. M. Blundell (San Francisco: ASP), in press
- Wilson, A. S., & Smith, D. A. 2002, *ApJ*, in preparation (Paper IV)
- Young, A. J., Wilson, A. S., Terashima, Y., Arnaud, K. A., & Smith, D. A. 2001, *ApJ*, submitted (Paper II)

Fig. 1.— An image of the central region of the Cygnus A field in the 0.75–8 keV band. The image has been “adaptively smoothed” with a 2-d Gaussian profile of varying width (see Section 3.1 for details). The shade is proportional to the square root of the intensity. The shading ranges from 0 (white) cts pixel⁻¹ to 15 (black) cts pixel⁻¹ (1 pixel is 0.''492 square). Filamentary features close to the nucleus, located at the center, are enhanced in this image.

Fig. 2.— The distribution of intracluster gas in an $\simeq 8' \times 8'$ region (i.e., chip S3) of the Cygnus A field in the 0.75–8 keV band. The background has been subtracted and the image convolved with a 2-d Gaussian profile of width $\sigma = 5$ pixels ($= 2.''46$). The vertical bar represents the relation between grey scale and cts pixel⁻¹ s⁻¹ cm⁻² (i.e. count rate corrected for variations in the effective area over the chip) in the convolved image.

Fig. 3.— An image of the whole *Chandra* field in the 0.75–8 keV band. The image has been binned to a pixel size of $3.''94 \times 3.''94$ and the parallel streaks on chip S4 resulting from read-out noise have been removed using the *CIAO* program DESTREAK. The vertical bar indicates the conversion from color to cts pixel⁻¹.

Fig. 4.— The radial profile of the intracluster gas in the 0.75–8 keV band. The data are shown (dots) together with the modeled isothermal β profile (solid line, see Section 3.2).

Fig. 5.— A color representation of the softness ratio (i.e., 1–2 keV/2–8 keV) in the region covered by the S3 chip superposed on X-ray contours of the background-subtracted image in the 0.75–8 keV band (see Section 3.3). The X-ray image has been adaptively smoothed with a 2-d Gaussian profile of varying width. The vertical bar indicates the relation between color and softness ratio, and the pixels were rebinned so that the fractional error in the ratio did not exceed 0.1. The contours indicate $2.5^n \times 10^{-2}$ cts pixel⁻¹, where $n = 1, 2, 3, 4, 5, 6, 7$, and 8.

Fig. 6.— A background-subtracted image of the Cygnus A field covered by the S3 chip in the 0.75–8 keV band. The image has been convolved with a 2-d Gaussian profile of width $\sigma = 5$ pixels ($= 2.''46$). The solid black lines mark regions from which spectra of the intracluster gas were extracted (see Table 1). The numbers of the annuli are indicated. The vertical bar represents the relation between grey scale and cts pixel⁻¹.

Fig. 7.— The spectrum of all the intracluster gas imaged on chip S3 (see Section 3.3). The upper panel shows the data together with the folded model (model 1, solid line, see Table 2). The residuals, in units of σ , from the best-fit absorbed mekal model are shown in the lower panel. The data have been binned so that the signal to noise ratio in each bin exceeds 10, but with no more than 10 spectral channels added together.

Fig. 8.— The observed properties of the intracluster gas in individual annuli (see Table 1 for the parameters of the ellipses or circles used for each annulus) surrounding the radio galaxy. For the elliptical annuli, the projected radius is the average of the semi-major and semi-minor axes of that annuli. (a) Gas temperature. (b) Metal abundance.

Fig. 9.— The deprojected properties of the intracluster gas in individual shells (see Table 1 for the parameters of the ellipsoids or spheres used for each shell) surrounding the radio galaxy. For each ellipsoidal shell, the radius is the average of the semi-major and semi-minor axis. Derived properties are not given for the outer shell for the reason given in Section 3.5. (a) Gas temperature (crosses) and electron density (solid line). (b) Metal Abundance (crosses) and thermal gas pressure (solid line).

Fig. 10.— The integrated mass profiles $M(< r)$ of the cluster (solid and dashed lines), assuming hydrostatic equilibrium and spherical symmetry, and the intracluster gas (dotted line) for radii between 80 and 500 kpc. The solid and dashed lines are for the centrally decreasing temperature profile, given by Equation 4 in Section 3.6, and the constant temperature profile, respectively.

Fig. 11.— An unsmoothed image of the central region of the Cygnus A field in the 0.75–8 keV band. The shade is proportional to the square root of the intensity. The shading ranges from 0 (white) cts pixel^{-1} to 15 (black) cts pixel^{-1} . Solid white lines mark regions from which spectra of extended X-ray emission were extracted (see Section 3.7).

Table 1. The boundaries of the individual annuli used for spectral analysis^a

Annulus	a^b (arcsec)	b^c (arcsec)	P.A. _{·maj} ^d (degrees)	P.A. _{·begin} ^e (degrees)	P.A. _{·end} ^f (degrees)
-	61.5	28.3	116.3
1	64.0	36.9	116.3	(0.0, 170.0)	(70.0, 220.0)
2	66.4	44.3	116.3	(0.0, 170.0)	(70.0, 220.0)
3	68.9	51.7	111.3	(0.0, 170.0)	(70.0, 220.0)
4	71.3	61.5	111.3	(0.0, 170.0)	(70.0, 220.0)
5	73.8	73.8	0	(0.0, 170.0)	(70.0, 220.0)
6	86.1	86.1	0	345.0	237.0
7	110.7	110.7	0	20.0	270.0
8	147.6	147.6	0	20.0	270.0
9	196.8	196.8	0	45.0	220.0
10	246.0	246.0	0	90.0	195.0
11	295.2	295.2	0	105.0	190.0
12	344.4	344.4	0	110.0	185.0

^aThe first row gives the semi-major, semi-minor axis, and orientation of the inner ellipse of annulus 1. All other values refer to the outer boundary of the corresponding annulus.

^bSemi-major axis of ellipse.

^cSemi-minor axis of ellipse.

^dP.A. of major axis of ellipse measured N through E.

^eP.A. of beginning angle(s) of partial ellipse(s).

^fP.A. of ending angle(s) of partial ellipse(s).

Table 2. Spectral fits to the integrated intracluster emission imaged on chip S3 in the 0.75–8 keV band.

Model	$N_{\mathrm{H}}^{\mathrm{a}}$ (10^{21} cm^{-2})	$kT_{\mathrm{l}}^{\mathrm{b}}$ (keV)	$Z_{\mathrm{l}}^{\mathrm{c}}$ (Z_{\odot})	$\mathrm{Norm}_{\mathrm{l}}^{\mathrm{d}}$ ($\frac{10^{-14}}{4\pi d_{\mathrm{A}}^2} \int n_{\mathrm{e}} n_{\mathrm{H}} dV$)	$kT_{\mathrm{h}}^{\mathrm{e}}$ (keV)	$Z_{\mathrm{h}}^{\mathrm{f}}$ (Z_{\odot})	$\mathrm{Norm}_{\mathrm{h}}^{\mathrm{g}}$ ($\frac{10^{-14}}{4\pi (d_{\mathrm{A}}(1+z))^2} \int n_{\mathrm{e}} n_{\mathrm{H}} dV$)	χ^2 (d.o.f.)
1	$2.815^{+0.075}_{-0.075}$	$8.26^{+0.37}_{-0.37}$	$0.346^{+0.051}_{-0.050}$	$(2.344^{+0.031}_{-0.031}) \times 10^{-2}$	736.2 (489)
2	$3.39^{+0.29}_{-0.28}$	$0.67^{+0.14}_{-0.04}$	1.0^{fixed}	$(3.1^{+1.6}_{-1.2}) \times 10^{-4}$	$7.66^{+0.44}_{-0.44}$	$0.336^{+0.048}_{-0.047}$	$(2.407^{+0.052}_{-0.040}) \times 10^{-2}$	709.4 (487)

^aMeasured column density.

^bLow temperature thermal component intended to represent spatially uniform Galactic emission.

^cMetal abundance of low temperature thermal component.

^dNormalization of the low temperature thermal component. d_{A} refers to the effective distance of this component. The units are c.g.s.

^eHigh temperature thermal component intended to represent cluster emission.

^fMetal abundance of high temperature thermal component.

^gNormalization of the high temperature thermal component. The units are c.g.s.

Note. — The errors given here are not strictly correct because both models provide unacceptable descriptions of the data (e.g., Lampton, Margon, & Bowyer 1976).

Table 3. Spectral fits to the observed emission from the annuli with a two-component mekal model and constant X-ray absorption in the 0.75–8 keV band.

Annulus ^a	N_{H}^{b} (10^{21} cm^{-2})	kT_{l}^{c} (keV)	Z_{l}^{d} (Z_{\odot})	$\text{Norm}_{\text{l}}^{\text{e}}$ ($\frac{10^{-14}}{4\pi d_{\text{A}}^2} \int n_{\text{e}} n_{\text{H}} dV$)	kT_{h}^{f} (keV)	Z_{h}^{g} (Z_{\odot})	$\text{Norm}_{\text{h}}^{\text{h}}$ ($\frac{10^{-14}}{4\pi (d_{\text{A}}(1+z))^2} \int n_{\text{e}} n_{\text{H}} dV$)	$\chi^2 \text{ (d.o.f.)}^{\text{i}}$
1	$3.109^{+0.083}_{-0.086}$	$0.593^{+0.07}_{-0.11}$	1.0 ^{fixed}	$(5.6^{+1.7}_{-1.4}) \times 10^{-7}$	$5.27^{+0.40}_{-0.40}$	$0.80^{+0.20}_{-0.18}$	$(1.347^{+0.065}_{-0.064}) \times 10^{-3}$	2083.7 (2021)
2	$(5.8^{+1.7}_{-1.5}) \times 10^{-7}$	$5.77^{+0.78}_{-0.53}$	$0.68^{+0.26}_{-0.23}$	$(8.00^{+0.47}_{-0.48}) \times 10^{-4}$...
3	$(6.8^{+2.0}_{-1.7}) \times 10^{-7}$	$6.45^{+0.85}_{-0.74}$	$0.72^{+0.36}_{-0.30}$	$(6.93^{+0.48}_{-0.49}) \times 10^{-4}$...
4	$(1.01^{+0.30}_{-0.26}) \times 10^{-6}$	$7.7^{+1.3}_{-1.1}$	$0.55^{+0.29}_{-0.27}$	$(7.94^{+0.45}_{-0.46}) \times 10^{-4}$...
5	$(1.44^{+0.43}_{-0.37}) \times 10^{-6}$	$6.69^{+0.99}_{-0.88}$	$0.42^{+0.25}_{-0.23}$	$(8.19^{+0.47}_{-0.47}) \times 10^{-4}$...
6	$(3.9^{+1.2}_{-1.0}) \times 10^{-6}$	$7.6^{+1.0}_{-0.7}$	$0.41^{+0.20}_{-0.18}$	$(1.606^{+0.065}_{-0.065}) \times 10^{-3}$...
7	$(9.4^{+2.8}_{-2.4}) \times 10^{-6}$	$7.11^{+0.62}_{-0.57}$	$0.32^{+0.13}_{-0.13}$	$(2.740^{+0.083}_{-0.086}) \times 10^{-3}$...
8	$(1.86^{+0.55}_{-0.47}) \times 10^{-5}$	$7.63^{+0.80}_{-0.61}$	$0.34^{+0.13}_{-0.13}$	$(3.242^{+0.096}_{-0.095}) \times 10^{-3}$...
9	$(2.31^{+0.69}_{-0.59}) \times 10^{-5}$	$8.5^{+1.1}_{-1.0}$	$0.30^{+0.20}_{-0.18}$	$(2.097^{+0.082}_{-0.082}) \times 10^{-3}$...
10	$(1.78^{+0.53}_{-0.45}) \times 10^{-5}$	$7.8^{+1.7}_{-1.3}$	$0.02^{+0.30}_{-0.02}$	$(1.062^{+0.037}_{-0.064}) \times 10^{-3}$...
11	$(1.76^{+0.52}_{-0.45}) \times 10^{-5}$	$7.6^{+1.9}_{-1.3}$	$0.65^{+0.57}_{-0.46}$	$(5.98^{+0.58}_{-0.57}) \times 10^{-4}$...
12	$(1.84^{+0.55}_{-0.47}) \times 10^{-5}$	$8.7^{+5.6}_{-2.5}$	$0.22^{+0.75}_{-0.22}$	$(4.66^{+0.42}_{-0.57}) \times 10^{-4}$...

^aDefined in Table 1 and Figure 6.

^bMeasured column density.

^cLow temperature thermal component intended to represent spatially uniform Galactic emission.

^dMetal abundance of low temperature thermal component.

^eNormalization of the low temperature thermal component. d_A refers to the effective distance of this component. The units are c.g.s.

^fHigh temperature thermal component intended to represent cluster emission.

^gMetal abundance of high temperature thermal component.

^hNormalization of the high temperature thermal component. The units are c.g.s.

ⁱThis is the value of χ^2 (d.o.f.) for the fit to all of the annuli.

Table 4. Deprojected temperatures, abundances, and emissivities from spectral fits in the 0.75–8 keV band.

Shell ^a	N_{H}^{b} (10^{21} cm^{-2})	kT_{l}^{c} (keV)	Z_{l}^{d} (Z_{\odot})	$\text{Norm}_{\text{l}}^{\text{e}}$ ($\frac{10^{-14}}{4\pi d_{\text{A}}^2} \int n_{\text{e}} n_{\text{H}} dV$)	kT_{h}^{f} (keV)	Z_{h}^{g} (Z_{\odot})	$\text{Norm}_{\text{h}}^{\text{h}}$ ($\frac{10^{-14}}{4\pi(d_{\text{A}}(1+z))^2} \int n_{\text{e}} n_{\text{H}} dV$)	χ^2 (d.o.f.)
1	3.109	0.593	1.0	5.6×10^{-7}	$4.91^{+0.62}_{-0.56}$	$0.89^{+0.35}_{-0.30}$	$(9.97^{+0.83}_{-0.82}) \times 10^{-3}$	2084.2 (2057)
2	5.8×10^{-7}	$4.9^{+1.7}_{-1.1}$	$0.70^{+0.76}_{-0.55}$	$(3.57^{+0.63}_{-0.61}) \times 10^{-3}$	1888.6 (1888)
3	6.8×10^{-7}	$5.6^{+1.4}_{-1.1}$	$0.95^{+0.86}_{-0.60}$	$(3.98^{+0.65}_{-0.65}) \times 10^{-3}$	1760.5 (1759)
4	1.01×10^{-6}	$9.2^{+10.4}_{-2.5}$	$0.66^{+0.81}_{-0.66}$	$(3.17^{+0.55}_{-0.41}) \times 10^{-3}$	1649.1 (1637)
5	1.44×10^{-6}	$5.4^{+2.2}_{-1.3}$	$0.45^{+0.68}_{-0.45}$	$(2.01^{+0.33}_{-0.32}) \times 10^{-3}$	1531.6 (1507)
6	3.9×10^{-6}	$8.5^{+3.5}_{-2.0}$	$0.59^{+0.64}_{-0.59}$	$(2.27^{+0.25}_{-0.25}) \times 10^{-3}$	1413.7 (1381)
7	9.4×10^{-6}	$6.7^{+1.3}_{-1.0}$	$0.29^{+0.29}_{-0.26}$	$(3.85^{+0.25}_{-0.26}) \times 10^{-3}$	1248.5 (1195)
8	1.86×10^{-5}	$7.0^{+1.1}_{-0.9}$	$0.39^{+0.23}_{-0.22}$	$(5.12^{+0.26}_{-0.26}) \times 10^{-3}$	937.0 (949)
9	2.31×10^{-5}	$9.3^{+3.4}_{-2.0}$	$0.32^{+0.47}_{-0.32}$	$(4.15^{+0.34}_{-0.33}) \times 10^{-3}$	626.2 (673)
10	1.78×10^{-5}	$7.6^{+3.6}_{-2.0}$	< 0.23	$(4.29^{+0.27}_{-0.27}) \times 10^{-3}$	395.3 (435)
11	1.76×10^{-5}	$6.9^{+3.8}_{-2.2}$	$1.3^{+2.3}_{-1.2}$	$(2.26^{+0.61}_{-0.62}) \times 10^{-3}$	225.3 (260)
12	1.84×10^{-5}	$8.7^{+5.0}_{-2.4}$	$0.22^{+0.75}_{-0.22}$	$(6.07^{+0.52}_{-0.74}) \times 10^{-3}$	100.6 (112)

^aEach shell is the volume between two prolate spheroids or spheres which project to give the annuli defined in Table 1 and Figure 6.

^bMeasured column density.

^cLow temperature thermal component intended to represent spatially uniform Galactic emission.

^dMetal abundance of low temperature thermal component.

^eNormalization of the low temperature thermal component. d_A refers to the effective distance of this component. The units are c.g.s.

^fHigh temperature thermal component intended to represent cluster emission.

^gMetal abundance of high temperature thermal component.

^hNormalization of the high temperature thermal component. Note that this parameter refers to volume contained between the two prolate spheroids. The units are c.g.s.

Table 5. Properties of the intracluster gas for each of the spheroidal or spherical shells.

Mean Radius ^a (kpc)	Volume (10 ⁷² cm ³)	F_X ^b (10 ⁻¹¹ erg cm ⁻² s ⁻¹)	L_X ^c (10 ⁴⁴ erg s ⁻¹)	n_e ^d (10 ⁻² cm ⁻³)	P_g ^e (10 ⁻¹⁰ erg cm ⁻³)	τ_c ^f (10 ¹⁰ yr)
72.0	0.0144	1.2	1.4	3.0	2.3	0.078
79.9	0.0164	0.42	0.46	1.7	1.3	0.15
87.3	0.0204	0.53	0.60	1.6	1.4	0.15
95.7	0.0328	0.45	0.53	1.1	1.6	0.32
105.9	0.0503	0.23	0.25	0.72	0.62	0.39
120.7	0.0900	0.31	0.36	0.57	0.77	0.61
148.6	0.274	0.45	0.52	0.43	0.46	0.77
195.0	0.708	0.63	0.72	0.30	0.34	1.1
260.0	1.68	0.55	0.64	0.18	0.27	2.2
334.3	2.77	0.49	0.56	0.14	0.17	2.7
408.6	4.13	0.35	0.41	0.084	0.093	3.0
482.9	—	0.85	0.89	—	—	—

^aFor each ellipsoidal shell, the mean radius is the average of the semi-major and semi-minor axis.

^bObserved 0.5–10 keV flux.

^cUnobscured 2–10 keV rest-frame luminosity, calculated assuming a luminosity distance of $d_L = 346.4$ Mpc.

^dDerived electron density.

^eDerived gas pressure.

^fDerived cooling time.

Table 6. Spectral fits to the extended filaments, bands of X-ray emission near the nucleus, and limb-brightened regions of the cavity, in the 0.5–10 keV band.

Region	N_{H}^{a} (10^{21} cm^{-2})	kT^{b} (keV)	Z^{c} (Z_{\odot})	Norm ^d ($\frac{10^{-14}}{4\pi(d_{\text{A}}(1+z))^2} \int n_{\text{e}}n_{\text{H}}dV$)	χ^2 (d.o.f.)
A	$3.57^{+0.21}_{-0.20}$	$5.59^{+0.72}_{-0.54}$	$0.70^{+0.22}_{-0.19}$	$(9.92^{+0.64}_{-0.61}) \times 10^{-4}$	152.7 (152)
B	$2.78^{+0.22}_{-0.18}$	$6.19^{+0.84}_{-0.90}$	$0.63^{+0.22}_{-0.20}$	$(8.70^{+0.60}_{-0.51}) \times 10^{-4}$	204.8 (148)
C	$3.15^{+0.24}_{-0.22}$	$3.89^{+0.42}_{-0.39}$	$0.84^{+0.27}_{-0.23}$	$(6.35^{+0.63}_{-0.56}) \times 10^{-4}$	117.9 (111)
D	$3.63^{+0.32}_{-0.29}$	$4.45^{+0.71}_{-0.56}$	$0.88^{+0.39}_{-0.31}$	$(4.08^{+0.48}_{-0.43}) \times 10^{-4}$	64.1 (71)
E	$3.11^{+0.29}_{-0.25}$	$3.79^{+0.45}_{-0.41}$	$0.80^{+0.28}_{-0.25}$	$(5.18^{+0.57}_{-0.49}) \times 10^{-4}$	89.3 (91)
F	$3.24^{+0.33}_{-0.28}$	$3.97^{+0.56}_{-0.54}$	$0.76^{+0.37}_{-0.29}$	$(3.79^{+0.49}_{-0.43}) \times 10^{-4}$	49.7 (70)
G	$3.53^{+0.35}_{-0.31}$	$4.48^{+0.69}_{-0.53}$	$0.97^{+0.45}_{-0.36}$	$(3.69^{+0.46}_{-0.43}) \times 10^{-4}$	87.5 (72)
H	$2.82^{+0.26}_{-0.24}$	$7.0^{+1.7}_{-1.1}$	$0.97^{+0.52}_{-0.42}$	$(4.39^{+0.44}_{-0.43}) \times 10^{-4}$	113.7 (87)
I	$3.76^{+0.31}_{-0.28}$	$4.43^{+0.55}_{-0.46}$	$1.39^{+0.52}_{-0.41}$	$(4.31^{+0.53}_{-0.50}) \times 10^{-4}$	85.9 (82)
J	$3.36^{+0.22}_{-0.21}$	$6.58^{+0.96}_{-0.94}$	$0.64^{+0.28}_{-0.24}$	$(7.66^{+0.53}_{-0.51}) \times 10^{-4}$	141.6 (132)

^aMeasured column density.

^bTemperature.

^cMetal abundance.

^dNormalization of the mekal model. The units are c.g.s.

This figure "f1.gif" is available in "gif" format from:

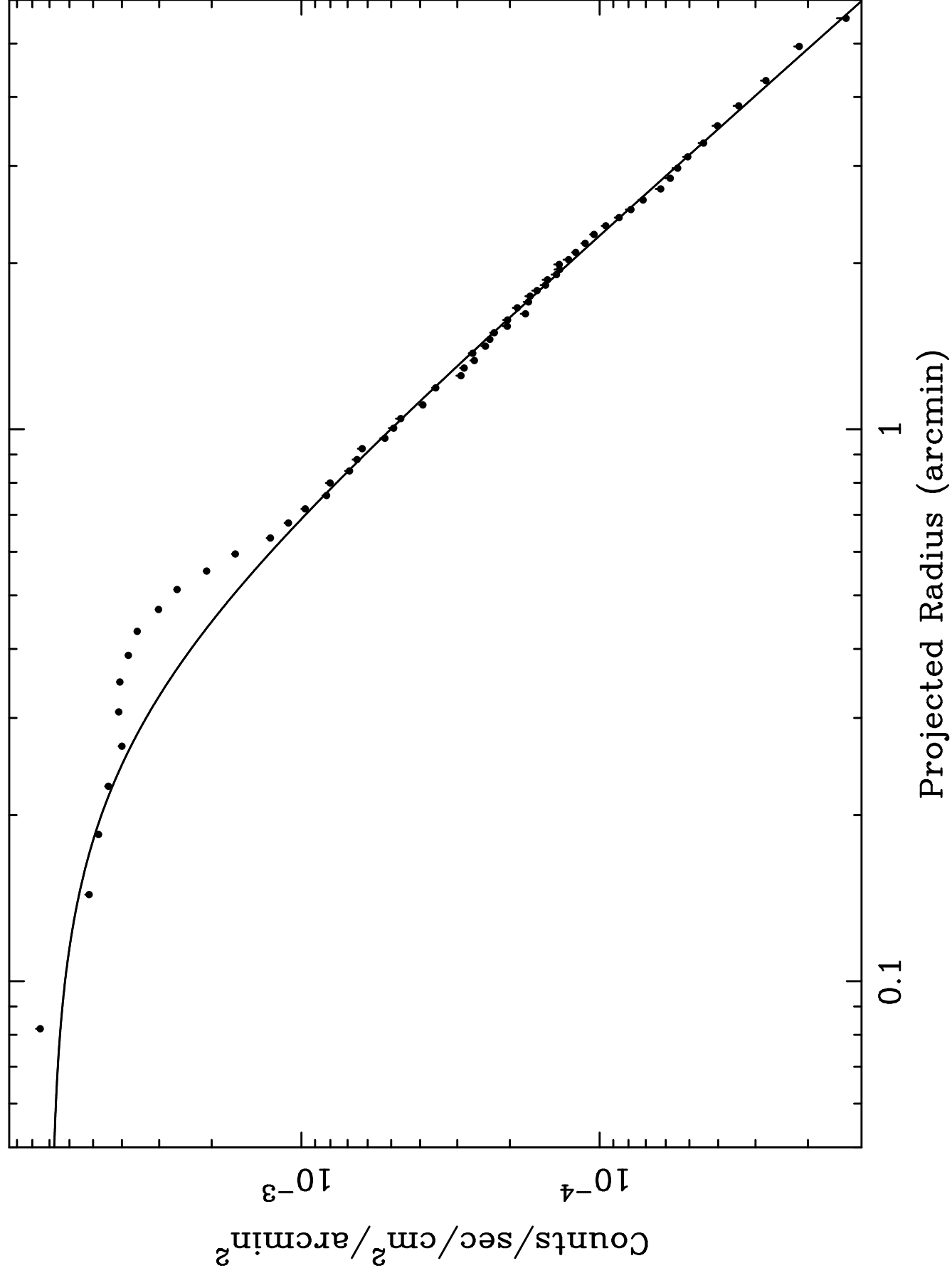
<http://arXiv.org/ps/astro-ph/0109488v1>

This figure "f2.gif" is available in "gif" format from:

<http://arXiv.org/ps/astro-ph/0109488v1>

This figure "f3.gif" is available in "gif" format from:

<http://arXiv.org/ps/astro-ph/0109488v1>

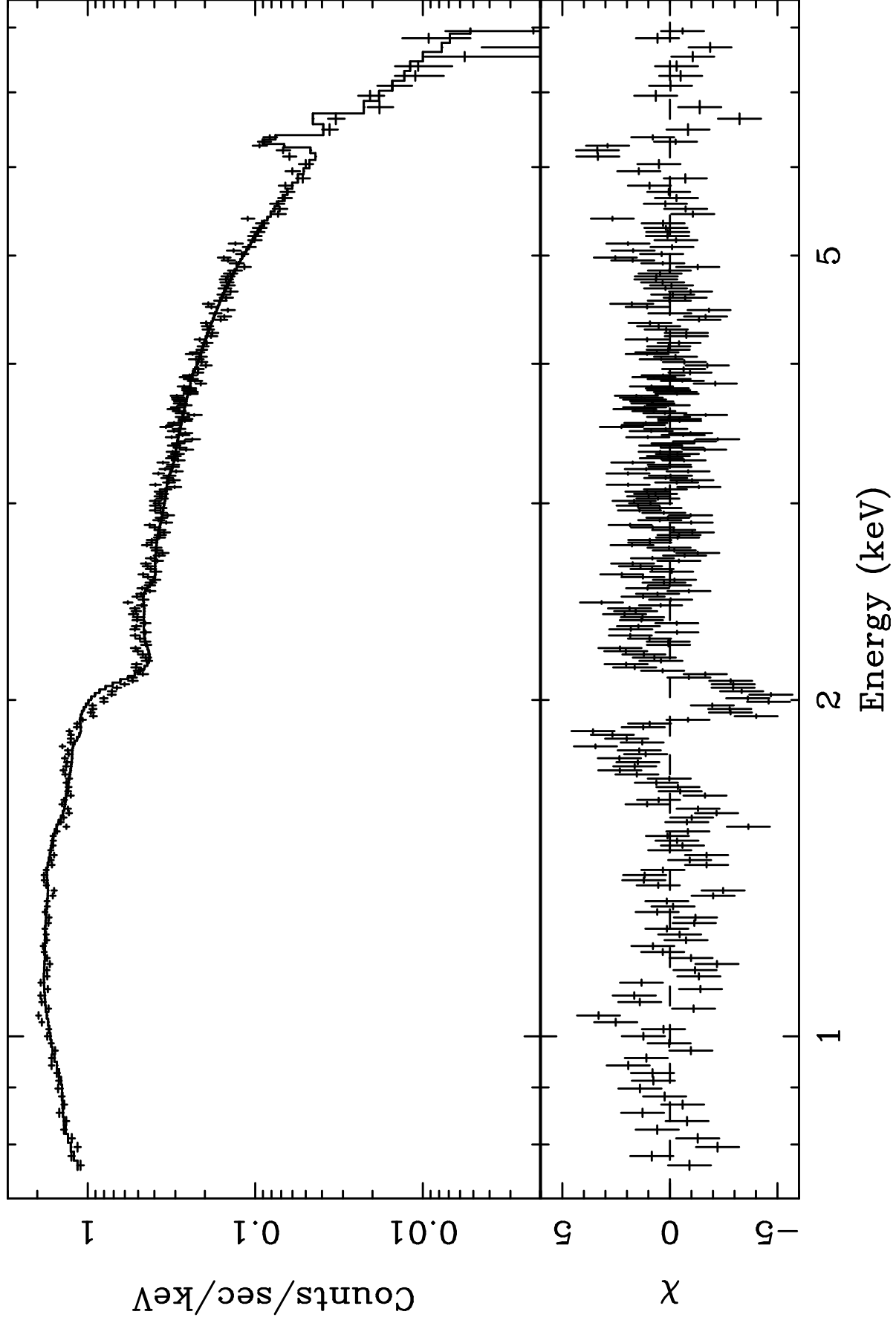


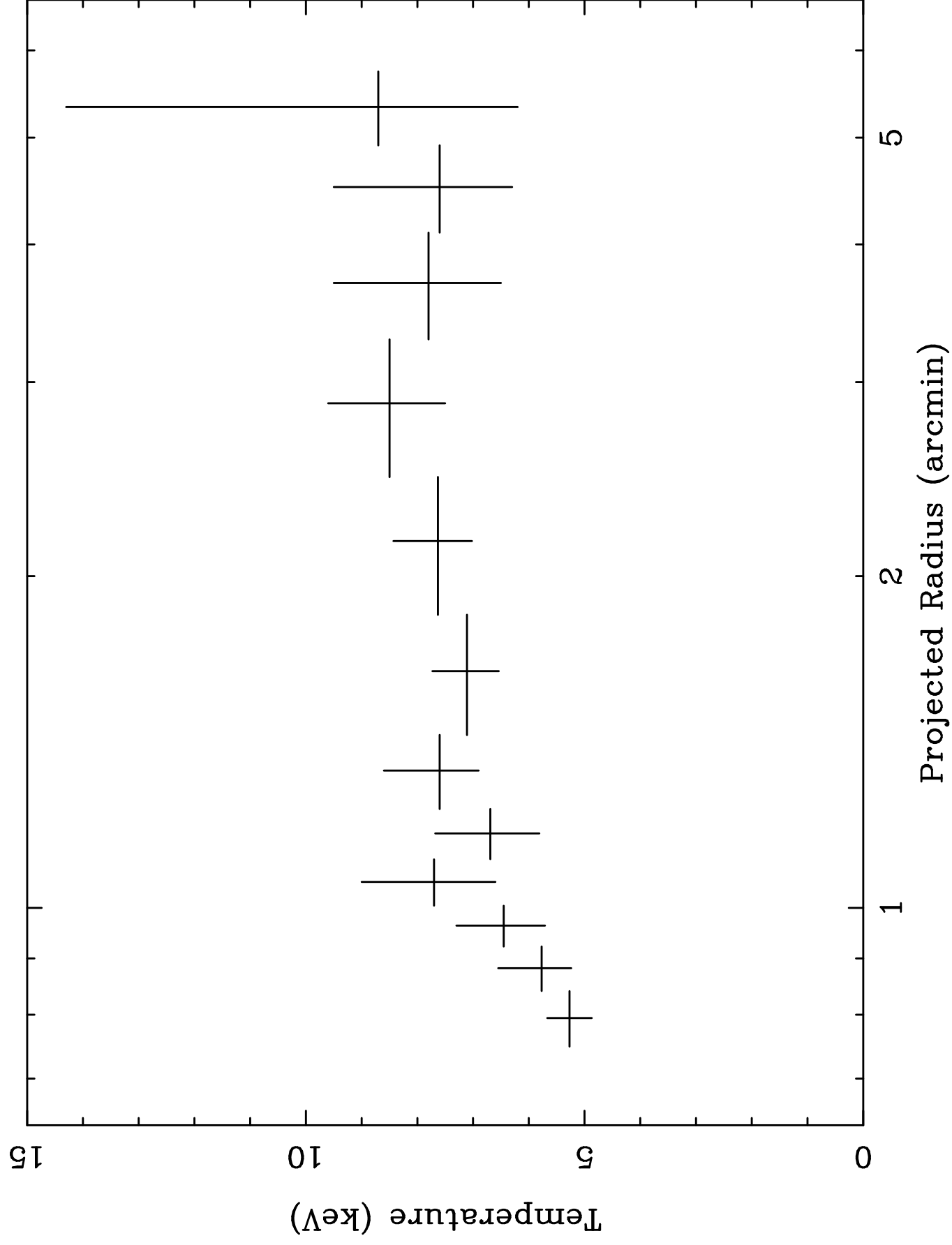
This figure "f5.gif" is available in "gif" format from:

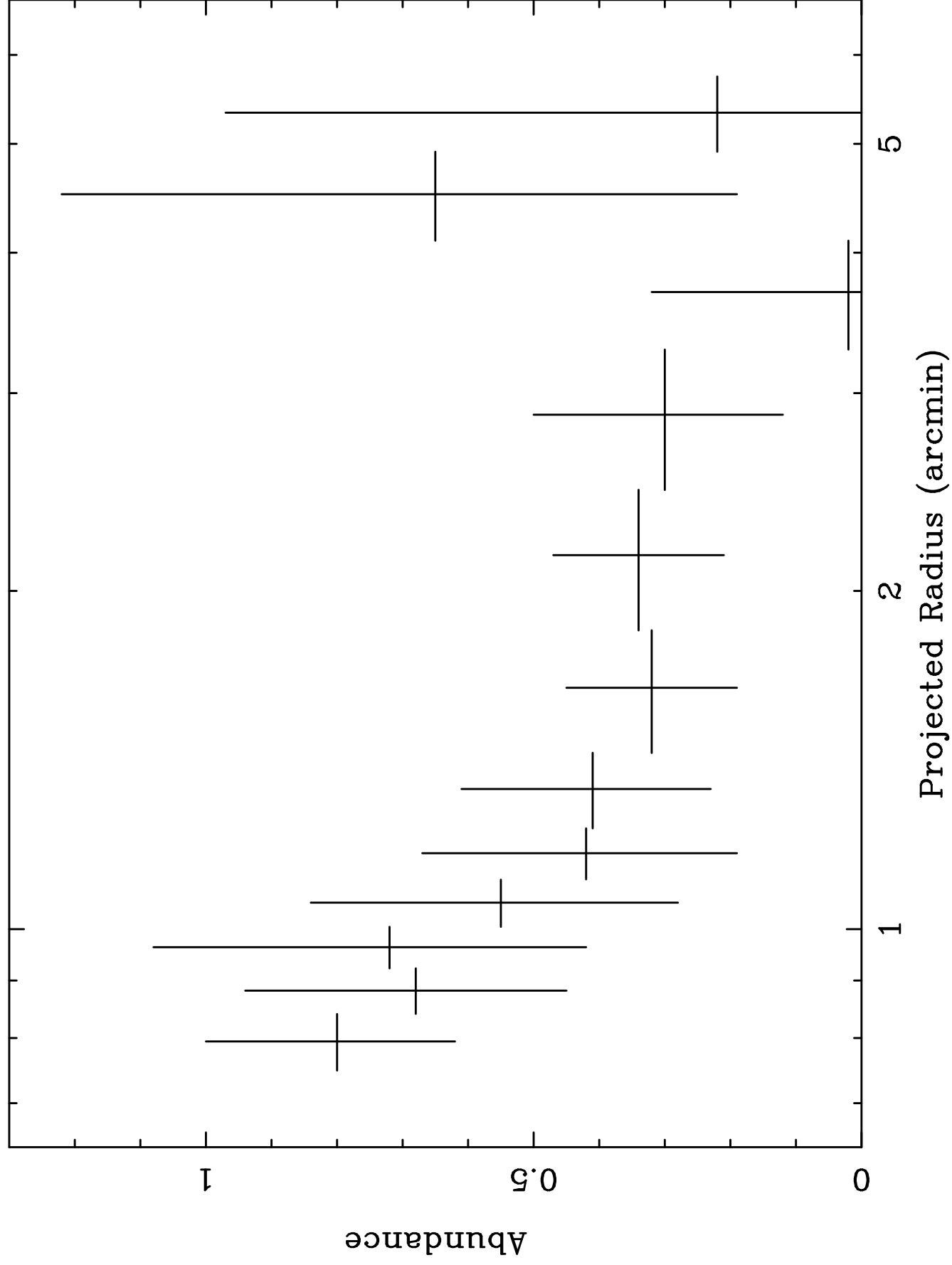
<http://arXiv.org/ps/astro-ph/0109488v1>

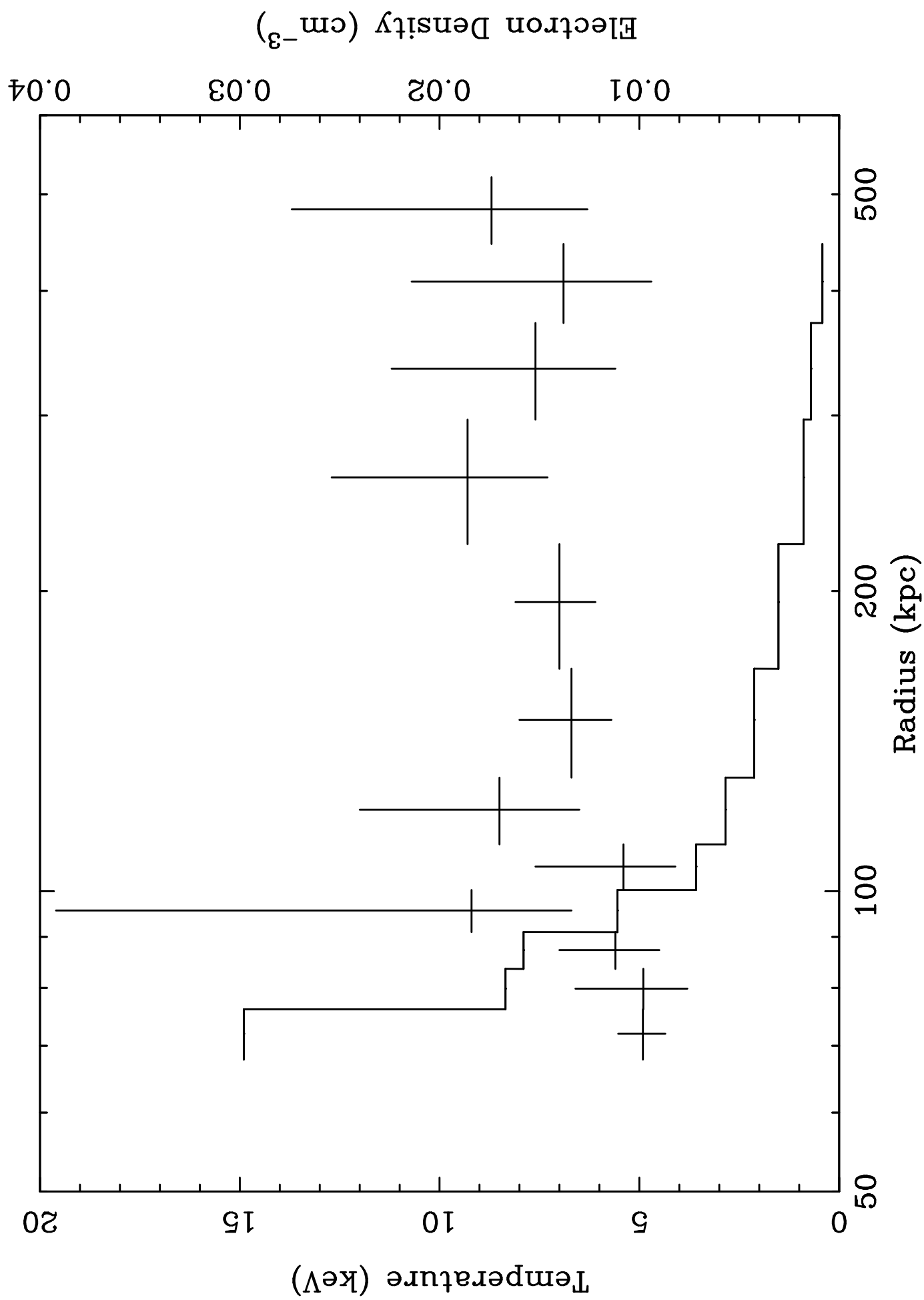
This figure "f6.gif" is available in "gif" format from:

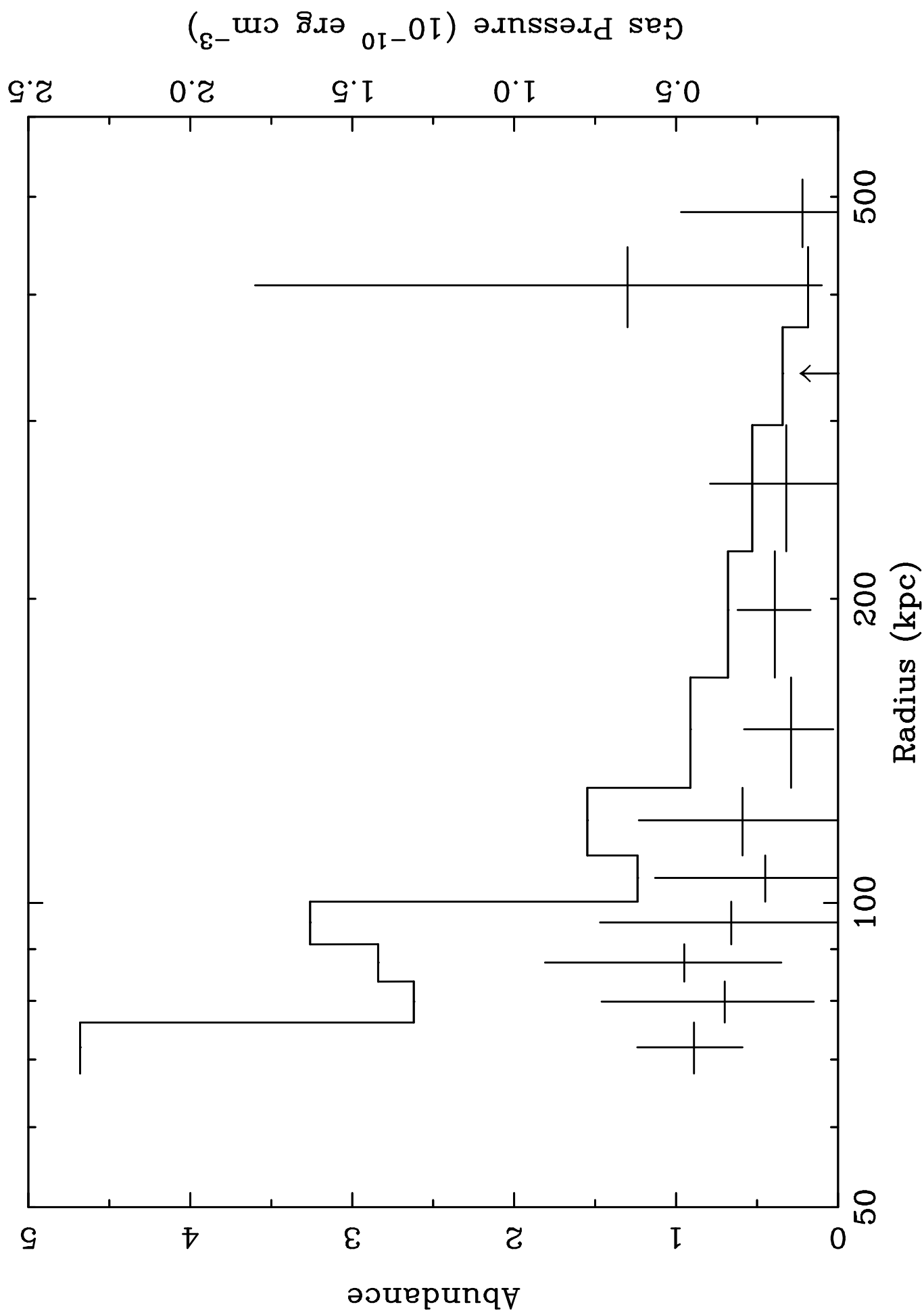
<http://arXiv.org/ps/astro-ph/0109488v1>

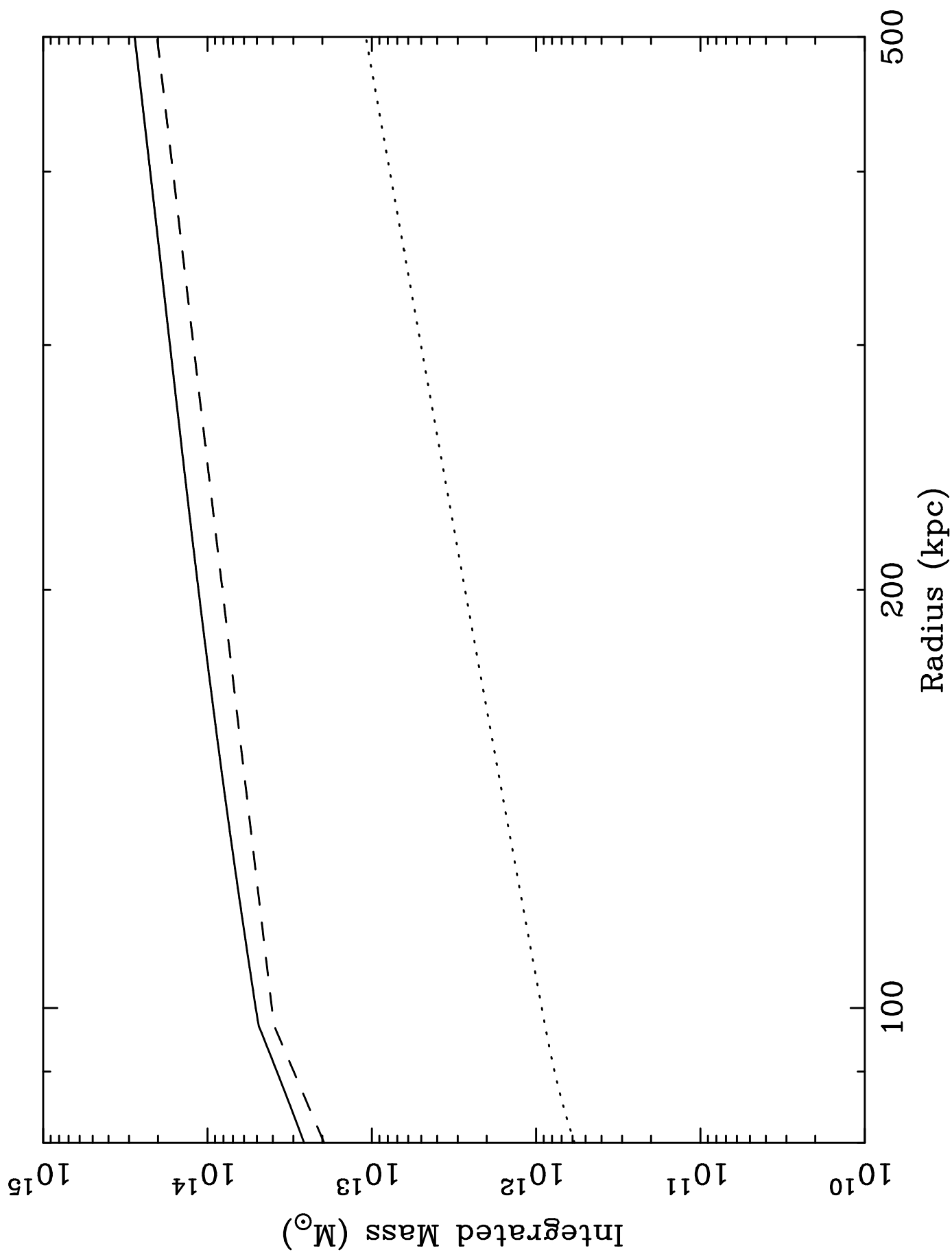












This figure "f11.gif" is available in "gif" format from:

<http://arXiv.org/ps/astro-ph/0109488v1>